Mass Transport Modifies the Interfacial Electrolyte to Influence Electrochemical Nitrate Reduction

Jinyu Guo,[†] Paige Brimley,[‡,⊥] Matthew J. Liu,[†] Elizabeth R. Corson,[†] Carolina Muñoz,[†] Wilson A. Smith,[‡,⊥] William A. Tarpeh[†,*]

†Department of Chemical Engineering, Stanford University, Stanford, CA, 94305, USA

‡Department of Chemical and Biological Engineering, University of Colorado Boulder, Boulder, CO, 80303, USA

⊥Renewable and Sustainable Energy Institute, University of Colorado Boulder, Boulder, CO, 80303, USA

*Corresponding author, Email: wtarpeh@stanford.edu Address: 443 Via Ortega, Room 387, Stanford, CA, 94305, USA. Telephone: 650-497-1324

Keywords: Diffusion–migration–reaction model, electrolyte effects, infrared absorption spectroscopy, reaction microenvironment, reactive nitrogen, sustainable ammonia manufacturing

ABSTRACT

The electrochemical nitrate reduction reaction (NO_3RR) can facilitate remediation of nitrate-polluted wastewater and sustainable production of ammonia. As an important component of the reaction microenvironment, the interfacial electrolyte substantially influences NO_3RR but remains underexplored. Mass transport modifies the interfacial electrolyte properties (e.g., pH, solute concentrations) and thus regulates NO_3RR activity and selectivity. In a representative flow-cell configuration with a titanium NO_3RR electrode, we systematically controlled mass transport conditions and demonstrated their impacts on NO_3RR performance. With continuum model simulation and *in situ* infrared absorption spectroscopy, we characterized the interfacial electrolyte environment under varied mass transport conditions. Furthermore, we strategically tuned the interfacial electrolyte properties and experimentally deconvoluted their impacts on NO_3RR activity and selectivity. We found that diffusion layer thickness and background electrolyte concentration govern NO_3RR activity, while interfacial pH steers NO_3RR selectivity. Inspired by these findings, we applied pulsed potential to periodically refresh the interfacial electrolyte environment and lower the local pH, successfully tripling the relative ammonia-to-nitrite selectivity. Distinct from NO_3RR studies that focus on reaction kinetics, this study was conducted under commonly observed mass transport limitations to advance mechanistic understanding behind mass transport effects and to help identify engineering opportunities that optimize ammonia production.

INTRODUCTION

Anthropogenic activities have imbalanced the global nitrogen cycle via large-scale Haber-Bosch ammonia manufacturing. The removal of reactive nitrogen species (all inorganic forms besides dinitrogen) has fallen far behind their production, leading to heavy environmental burdens and continuous losses from the nitrogen economy. As the most prevalent waterborne reactive nitrogen pollutant, excessive nitrate (NO_3^-) jeopardizes both human and ecosystem health.[1–7] Meanwhile, the reactive nature of nitrate presents a promising opportunity to transform it into other value-added nitrogen products via the electrochemical nitrate reduction reaction (NO_3RR). One representative product is ammonia (NH_3), a widely used commodity chemical, green energy carrier, and fertilizer component. By leveraging renewable energy, electrochemical NO_3RR enables nitrate-polluted water remediation and sustainable ammonia production. Distributed electrochemical NO_3RR can reduce transportation costs embedded in traditional centralized wastewater treatment and chemical manufacturing, and help address spatial and temporal imbalances in the nitrogen cycle.[8–10]

In ongoing efforts to improve activity and ammonia selectivity of electrochemical NO_3RR, researchers have mainly focused on improving electrocatalysts. However, it has been increasingly recognized that the *reaction microenvironment*, which contains both the electrocatalyst and the interfacial electrolyte between the electrocatalyst and the bulk electrolyte, directly influences electrocatalytic reduction reactions (e.g., carbon dioxide reduction reaction, CO_2RR; oxygen reduction reaction, ORR; hydrogen evolution reaction, HER).[11–20] Specifically, the interfacial electrolyte is composed of a compact electrical double layer (EDL) that extends a few nanometers away from the electrode surface, and a diffusion layer that spans up to a few hundred microns into the bulk electrolyte.[21] As the immediate environment where reactions take place, the interfacial

electrolyte physicochemical properties (e.g., electric potential, pH, solute concentrations) may differ drastically from the bulk.[11,17,22] Among these properties, electric potential serves as the thermodynamic driving force for electrode reactions, and pH indicates the abundance of proton sources, both of which influence reaction activity and selectivity. In terms of ionic solutes, coexisting anions (e.g., Cl^-, SO_4^{2-}) can compete with reactant nitrate for surface sites and affect activity; and cations (e.g., Na^+, K^+) are known to interact with reaction intermediates, as well as modify the interfacial electric field and pH, thus influencing activity and selectivity.[13,23,24] Although the effects of bulk electrolyte properties on electrochemical NO_3RR have been reported,[5,25–27] few studies have explicitly investigated the interfacial electrolyte environment during reaction,[28] much less its impacts on NO_3RR activity and selectivity. This gap in understanding is largely due to the micron-scale and dynamic nature of the interfacial electrolyte environment, which makes it inherently challenging to probe experimentally.[15,16,22] To this end, computational simulations using continuum models have shown promise as a high-fidelity, computationally efficient approach to describe interfacial electrolyte properties.[29–32]

Although their physicochemical properties differ, the interfacial and bulk electrolytes are bridged by mass transport phenomena. During electrochemical NO_3RR, the anionic reactant nitrate must travel against the electric field generated by the often negatively charged electrode and specifically adsorb to the electrode surface. A broad, multiphase portfolio of products can be generated at the electrode (e.g., hydroxide ions, nitrite, dinitrogen, ammonia), many of which can undergo homogeneous acid–base reactions and in turn influence the interfacial electrolyte environment.[33] Meanwhile, HER competes with NO_3RR and contributes to modifying the interfacial electrolyte environment. Because mass transport governs the supply of reactant and dissipation of products,

it influences interfacial electrolyte properties that impact the activity of NO_3RR and concurrent HER, as well as the selectivity of NO_3RR (altogether referred to here as NO_3RR performance). In both fundamental studies and large-scale applications, mass transport often limits NO_3RR activity,[9,34]and was found to impact NO_3RR selectivity.[35,36] However, current understanding of their underlying mechanisms remains insufficient for informing process engineering. More broadly, several characteristics of NO_3RR make it a suitable "model reaction" to study mass transport effects in electrocatalytic reduction reactions: (1) improved control of reactant speciation and concentration, compared to e.g., CO_2RR ($CO_{2(g)}$ vs. $CO_{2(aq)}$ vs. $H_2CO_{3(aq)}$)[35–40]; (2) enhanced opportunities to investigate reaction selectivity, compared to e.g., HER; and (3) sufficient but not prohibitive complexities for computational simulations. Therefore, we purposely imposed (rather than minimized, as required in reaction kinetic studies) the mass transport limitation to elucidate mass transport effects in NO_3RR. We systematically controlled the extent of mass transport and investigated: (1) how mass transport influences NO_3RR performance, (2) how mass transport modulates the interfacial electrolyte environment, and (3) how properties of the interfacial electrolyte environment impact the reaction activity and selectivity.

Recognizing the pivotal role of the interfacial electrolyte environment, we approached the mass transport effects from a microscopic perspective by combining electrochemical experiments, continuum model simulations, and spectroscopic characterizations. We conducted electrochemical experiments in a representative and translational membrane-separated flow cell, using planar polycrystalline titanium (Ti) foil as a generic NO_3RR electrode. We imposed the mass transport limitation with a sufficiently negative applied potential; by varying the electrolyte flow rate, we tuned the extent of mass transport and evaluated its influence on NO_3RR performance. A

diffusion–migration–reaction model (generalized-modified Poisson–Nernst–Planck, GMPNP) was employed to simulate the interfacial electrolyte properties and illustrate their dependence on mass transport. Using experimental electrochemical data as model inputs, spatial profiles of electric potential and species concentration under the investigated flow conditions were resolved. Informed by this descriptive model, we further deconvoluted effects of interfacial pH and background electrolyte concentration by conducting flow cell experiments under varied bulk electrolyte properties and measuring *in situ* pH with the aid of attenuated total reflectance–surface-enhanced infrared absorption spectroscopy (ATR–SEIRAS). We found that enhanced mass transport promotes NO_3RR activity by promoting the diffusion of nitrate, but lowers ammonia selectivity by increasing the interfacial pH, exhibiting an activity–selectivity trade-off. Situated in NO_3RR, this study illustrates microscopic mechanisms of mass transport effects, and also provides broadly applicable insights on the role of mass transport in defining the reaction microenvironment in energy-relevant electrocatalytic reduction reactions.

METHODS

Electrochemical nitrate reduction experiments and product analysis

All electrochemical NO_3RR experiments were conducted in a custom airtight system consisting of a two-chamber membrane-separated flow cell and an electrolyte reservoir, unless otherwise specified. The electrolyte was recirculated between the electrochemical flow cell and the electrolyte reservoir; the electrolyte flow rate was controlled by peristaltic pumps (**Fig. S1** in **Supporting Information, SI**). A three-electrode configuration was always employed, consisting of a Ti working electrode (5.4 cm^2 geometric area), a platinum counter electrode, and a Ag/AgCl reference electrode; all potentials were converted to the reversible hydrogen electrode (RHE) scale

using the initial measured bulk pH. A cation exchange membrane (Nafion) separated the working and counter electrode chambers. All electrochemical experiments were conducted using 85% IR compensation, and all current densities reported were based on geometric electrode area.

For each NO_3RR experiment, identical electrolytes were added to the working and counter electrode chambers. Before and after each experiment, electrolytes from both chambers were sampled for pH measurement and aqueous product analysis. Nitrate and nitrite concentrations were quantified using anion chromatography, and ammonia concentration was quantified using spectrophotometric flow injection analysis.[41] Because homogeneous acid–base equilibria exist in the electrolyte, we reported the sum concentrations of conjugate acid–base pairs: nitrite refers to the sum of nitrite and nitrous acid, and ammonia refers to the sum of ammonia and ammonium. Gaseous products (H_2 and N_2) were analyzed by in-line gas chromatography. N_2 was not detected with a lower detection limit of 50 ppm (corresponding to 0.091 mA/cm^2 partial current density). Complementary experimental details are given in SI **Section S1.1–1.2**.

For each NO_3RR reaction condition (listed in **Table S3)**, triplicate experiments were performed, and the average and standard deviation were shown for all reported values. For all liquid samples from each NO_3RR experiment, triplicate measurements were conducted, and the average was used in calculating performance metrics. Total and product partial current densities, time-averaged nitrate removal rate, Faradaic efficiency (FE), and nitrogen selectivity (N-selectivity) were used as key metrics to assess NO_3RR performance (definitions in SI **Section S1.3**). Control experiments

were conducted to confirm negligible contamination and detection noise in ammonia production (SI **Section S1.8**).

Continuum model summary

To simulate interfacial electrolyte properties under NO_3RR reaction conditions, we adapted the GMPNP originally developed for CO_2RR,[29] because of several advantages: (1) the continuum treatment of the electrolyte circumvents the prohibitively high computational cost of *ab initio* simulations for regions larger than the nanometer scale, (2) the inclusion of migration enables the reconstruction of the EDL and illustrates how different time scales govern bulk and interfacial phenomena, which the reaction–diffusion model fails to capture, and (3) the inclusion of solvated species sizes to the PNP model facilitates derivation of physically relevant concentration profiles (i.e., below the steric limit).[29–32]

The physical regions simulated in the GMPNP model are depicted in **Fig. 2a**. This descriptive model simulated the time-dependent, one-dimensional electric potential and species concentration profiles outside of the outer Helmholtz plane (OHP). The reactive transport of species within the simulation zone was calculated via the generalized-modified Nernst–Planck equations, the potential was treated with the Poisson equation, and the two sets of equations were solved self-consistently using the continuity equation. Primary reactions and model parameters are summarized in SI **Section S2.1**, and the governing equations were non-dimensionalized to improve numerical stability and computational efficiency. We used Dirichlet boundary conditions for the potential to be an integer multiplier of the thermal voltage referenced to the potential of zero charge

(PZC) of the electrode at the OHP, as well as for species concentrations at the right-hand boundary at the diffusion layer edge. The DFT-calculated PZC of the most likely surface species under reaction conditions, TiH_2, was used (–0.9 V_{RHE}).[42] To simulate interfacial electrolyte properties under varying mass transport conditions, the corresponding equivalent diffusion layer thickness, δ_{eqv}, and product partial current densities from NO_3RR experiments were used as Neumann boundary conditions at the OHP (**Fig. S10** and **Table S8**).

The simulation time was chosen to be sufficient to fully establish the EDL (i.e., charge density within the EDL converged, the potential profile was unchanging, and concentration of all ionic species change within 0.1% between timesteps). Because of the right-hand Dirichlet boundary conditions, a true steady state is difficult to achieve, and we refer to this condition as "pseudo-steady state"(SI **Section S2.3**). As demonstrated by Bohra et al., the autoionization of water is out of equilibrium within the EDL (i.e., $[H^+]\cdot[OH^-] \neq K_W$, 1.01×10^{-14} at 25 °C),[29] likely due to the neglected ion-ion interactions beyond steric effects within the GMPNP equations and the pseudo-steady-state condition within our simulations. Therefore, we defined pH-equivalent (**Eqn. S28**) to quantitatively describe the interfacial electrolyte environment, which converts the relative abundance of H^+ and OH^- into a value equivalent to the classical pH value under the same condition. Limitations of the GMPNP models are also discussed in SI **Section S2.4**.

Local pH measurement using ATR–SEIRAS

We used attenuated total reflectance−surface-enhanced infrared absorption spectroscopy (ATR–SEIRAS) to measure the interfacial pH under NO_3RR conditions. Because Ti does not exhibit the surface enhancement effect,[43] a thin layer of copper (Cu, < 100 nm) was deposited onto a germanium crystal for use as the working electrode in ATR–SEIRAS experiments in a custom single-chamber, three-electrode electrochemical cell. *In situ* pH measurements were performed in acidic and neutral phosphate buffer electrolytes during chronoamperometry experiments, and the local pH was determined using a ratio of peak areas from the phosphate species (calibration range pH 1–13.5). Details on the ATR–SEIRAS cathode fabrication, pH calibration, and *in situ* pH measurement are given in SI **Section S1.9**.

RESULTS AND DISCUSSION

How does mass transport influence the activity of NO_3RR and HER and the selectivity of NO_3RR?

To systematically examine mass transport effects in NO_3RR, we first quantified the dependence of mass transport conditions on flow conditions. We used a flow cell to enable facile product quantification under varying mass transport conditions and to provide translational insights towards continuous-flow implementation. Flow cell results were related to rotating disk electrode (RDE) experiments using an equivalent diffusion layer thickness measured at a series of electrolyte flow rates (see SI **Section S1.4**). As expected, δ_{eqv} generally decreased with increasing flow rate (**Fig. 1a**). Although all flow rates studied corresponded to laminar flow, three distinguishable δ_{eqv} regimes were observed: a drastic decrease in δ_{eqv} under low flow rates, a nearly constant δ_{eqv} under medium flow rates, and a gradually decreasing δ_{eqv} under high flow rates, approaching 65

μm at the flow rate of 113 mL/min (maximum flow rate without causing electrolyte leakage). Notably, this highest accessible flow rate translates to an RDE rotation rate of below 50 RPM in a typical setup (15 mm disk outer diameter), highlighting that the flow cell facilitates investigation of mass transport conditions in the low-mixing region with higher resolution than RDE. Five electrolyte flow rates (flow rates I to V, from 11.5 to 101.5 mL/min, **Table S1**) spanning all three regimes were thus applied in NO_3RR experiments.

We isolated the effects of mass transport by keeping several parameters constant across our experiments, including the NO_3RR electrocatalyst, initial nitrate concentration, background electrolyte, and applied potential. Polycrystalline Ti was used as a generic NO_3RR electrocatalyst because of its appreciable NH_3 selectivity, abundance, moderate cost, and corrosion resistance.[25,42] We used 10 mM nitrate to reflect our application goal of treating dilute nitrate-polluted feedstocks (e.g., municipal wastewater, agricultural runoff) as opposed to the wide range of commonly used nitrate concentrations in NO_3RR literature (0.1–1.0 M; see SI **Section S1.5**).[4,9,44] The background electrolyte was fixed as $NaClO_4$ (with varied concentrations) to leverage a weakly adsorbing anion (ClO_4^-) that minimizes surface site blocking,[45,46] and a common wastewater cation (Na^+) with moderate ion size and acidity to represent cation effects.[23,47] We performed potentiostatic experiments at a sufficiently negative value (–1.0 V_{RHE}, see SI **Section S1.7**) where NO_3RR is not kinetically limited under the five designated flow rates. We first examined the flow rate dependence of NO_3RR performance (i.e., activity of NO_3RR and HER and selectivity of NO_3RR) in 1 M $NaClO_4$ + 10 mM HNO_3 electrolyte (referred to as the concentrated background). To prevent the possible influence of electrolyte flow rate on reaction progress,[48,49] a fixed

recirculation event number was used across different flow rates (i.e., reaction duration inversely proportional to flow rate, **Table S9**).

NO_3RR activity, as captured by the time-averaged nitrate removal rate, generally increased with increasing flow rate (**Fig. 1b**). This activity trend confirmed that NO_3RR was subject to mass transport limitations under this applied potential across all five flow rates. Under a higher flow rate, a thinner diffusion layer posed less mass transport resistance, leading to a faster delivery of reactant to the electrode surface and a higher reaction rate. We further confirmed that NO_3RR activity was limited by the mass transport of nitrate (with experiments using an elevated nitrate concentration, SI **Section S3.1.2**). In contrast to the monotonic trend of NO_3RR activity with respect to flow rate, the activity of the competing HER (captured by the H_2 partial current density) did not show clear flow rate dependence (**Fig. S14**). Combined with cyclic voltammetry features (**Fig. S5**), this independence indicated that water reduction was the main HER mechanism under the applied potential (–1.0 V_{RHE}) because the concentration of reactant water was not affected by mass transport conditions. Additionally, despite operation at a very negative potential and a dilute nitrate concentration (10 mM), HER only comprised at most 14% FE (**Fig. 1c**). Because NO_3RR dominated, the total current density followed the same monotonic trend with flow rate as nitrate removal rate.

For NO_3RR selectivity, two observations were shared across all flow rates (**Fig. 1d**). First, nitrite and ammonia accounted for almost all NO_3RR products (combined N-selectivity approximately 100%. Second, nitrite was the majority nitrogen product (i.e., N-selectivity$_{NO_2^-}$ > 50%). However,

the distribution between the two nitrogen products (N-selectivity$_{NH_3}$/N-selectivity$_{NO_2^-}$, magenta symbols in **Fig. 1d**), changed slightly with flow rate, with NO_3RR favoring ammonia more under the lowest flow rate than under the highest flow rate. Because nitrite is a reaction intermediate in the reduction of nitrate to ammonia, we conducted long-duration experiments (250 min, SI **Section S3.1.3**) and confirmed that the observed N-selectivity trend held and was independent of the reaction time (**Fig. S18**). Taken together, the flow rate dependence of NO_3RR selectivity implied that the interfacial electrolyte environment was modified by mass transport and in turn influenced further reduction from nitrite to ammonia. Experiments were repeated under all five flow rates for a fixed reaction duration of 30 min, and similar activity and selectivity trends were established (SI **Section S3.1.4**). We therefore kept the reaction time as 30 min in subsequent potentiostatic experiments.

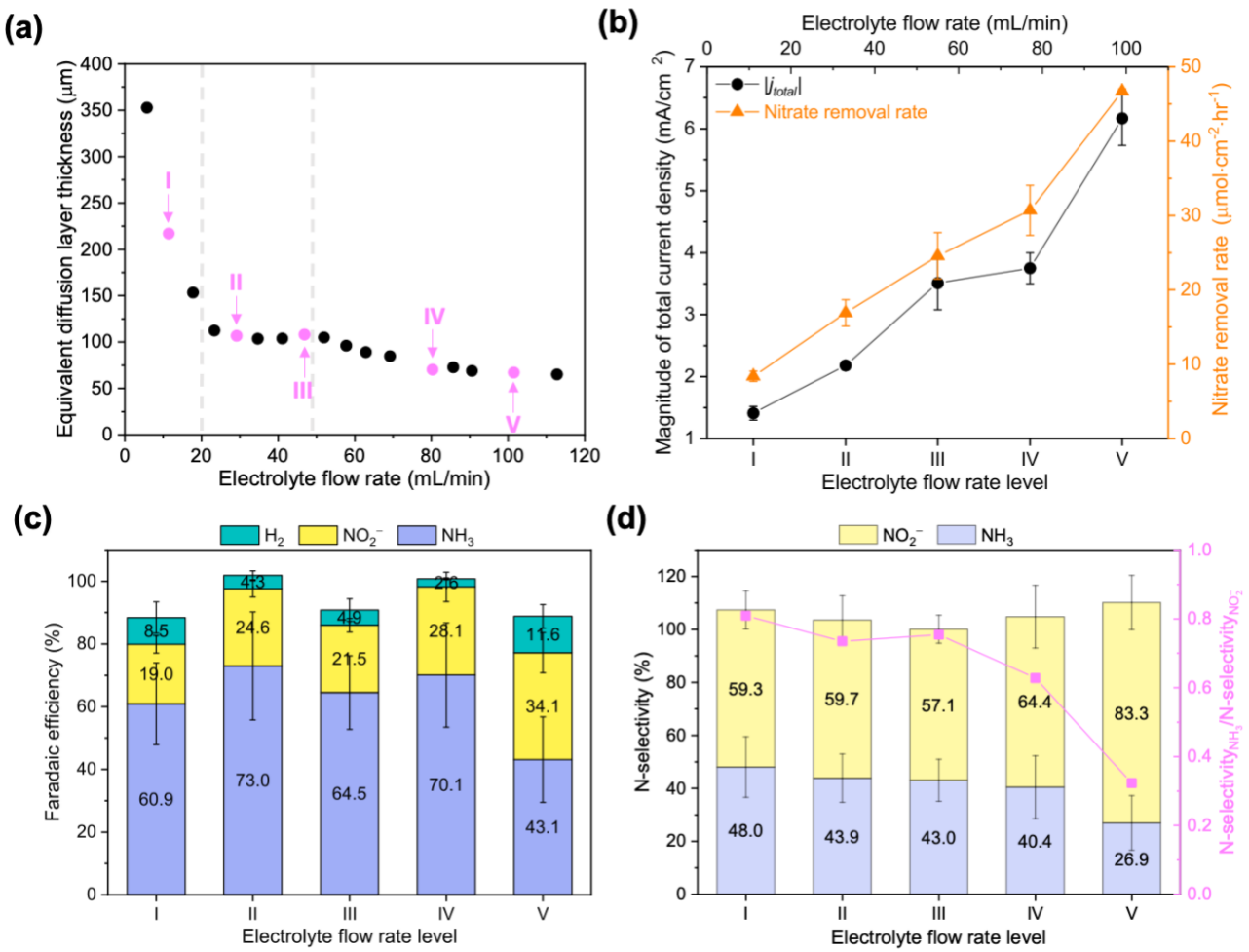

Fig. 1 Experimental demonstration of mass transport effects in NO_3RR. (a) Empirically determined equivalent diffusion layer thickness as a function of electrolyte flow rate. Three distinct regimes are segmented by dashed lines. Flow rates applied in electrochemical NO_3RR experiments are highlighted in magenta. Detailed values are tabulated in **Table S1**. **(b)** Absolute value of total current density (left axis) and time-averaged nitrate removal rate (right axis), **(c)** Faradaic efficiency, and **(d)** N-selectivity (left axis) and ammonia to nitrite N-selectivity ratio (magenta squares, right axis) as functions of the electrolyte flow rate. Potentiostatic experiments were conducted in 1 M $NaClO_4$ + 10 mM HNO_3, at –1.0 V_{RHE} for 90 recirculation events (experiment

durations in **Table S9**). Error bars represent ± one standard deviation. Error bars on N-selectivity ratios are given in **Fig. S15**.

How does mass transport modulate the interfacial electrolyte environment?

Elucidating experimentally observed effects of mass transport on NO_3RR performance requires a microscopic perspective of the interfacial electrolyte environment. We adapted the GMPNP model, which has successfully described CO_2RR in non-dilute electrolyte (>10 mM),[29] to characterize the interfacial electrolyte environment outside of the OHP under NO_3RR conditions. The empirically determined diffusion layer thickness and product partial current densities from potentiostatic NO_3RR experiments in the concentrated background (**Fig. 1**) were used as model inputs. GMPNP simulations output the spatial distribution of electric potential, background electrolyte species, NO_3RR reactants and products, and pH-equivalent at pseudo-steady state under the flow rates studied (model details in **Methods**).

Moving from the OHP to the bulk, the simulated electric potential logarithmically extinguishes to zero within approximately 2 nm (**Fig. S21a, b**), which corresponds to the diffuse layer. Within the same region, the background cation (Na^+) concentration decays from 4.3 M (the steric limit) to its bulk value of 1 M (**Fig. 2b**). The aggregation of cations at the OHP is due to their electrostatic attraction to the cathode and has been observed both computationally[13,50,51] and experimentally.[52] The resultant high local cation concentration can substantially impact reaction activity and selectivity by interacting with reaction intermediates or modifying the interfacial electric field and pH;[13,23,24,27,53] however, their putative molecular mechanisms cannot be explicitly simulated using

303 the GMPNP model alone. Nevertheless, the fact that Na^+ concentration profiles do not differ
304 appreciably across all flow rates (**Fig. S21c, d**) suggests that the aggregation of Na^+ influences
305 NO_3RR similarly across mass transport conditions. Converse to Na^+, the background anion (ClO_4^-)
306 concentration is lower in the EDL than in the bulk due to electrostatic repulsion and does not
307 change with flow rate (**Fig. S22a, b**). With much higher bulk concentrations than other ionic
308 species, Na^+ and ClO_4^- are the major constituents of the EDL. From the bulk to the OHP, the nitrate
309 concentration first declines gradually in the diffusion layer and then drops sharply by an order of
310 magnitude within the EDL (**Fig. 2b**, **Fig. S22c**), due to its consumption during NO_3RR and
311 electrostatic repulsion with the cathode (similar to ClO_4^-). Although the GMPNP model does not
312 describe the region within the OHP, the near-complete depletion of nitrate in the diffuse layer
313 rationalizes the observation that NO_3RR is subject to mass transport limitations for nitrate.

314

315 The experimentally observed basification phenomenon is also reproduced in GMPNP simulations.
316 The pH-equivalent profile exhibits a non-monotonic trend traversing simulated regions (**Fig. 2c**):
317 within the diffuse layer, the pH-equivalent is the lowest at the OHP, suggesting that the
318 electrostatic repulsion of OH^- outweighs its production in both heterogeneous and homogeneous
319 reactions; beyond the relative maximum at *ca.* 2 nm outside the OHP, the pH-equivalent decreases
320 to its bulk value in the diffusion layer. Under higher flow rates, the pH-equivalent profile is
321 uniformly higher across all simulated regions. Although simulated pH-equivalent values do not
322 equal actual pH values under input reaction conditions due to the pseudo-steady-state assumption,
323 a clear trend is established: a higher flow rate generates a more alkaline local environment,
324 suggesting that the intensified production of OH^- outpaces its intensified dissipation. Because the

trends for pH-equivalent and N-selectivity$_{NH_3}$/N-selectivity$_{NO_2^-}$ coincide, we hypothesized that the interfacial pH mediates the distribution between the two nitrogen products.

In addition to OH^-, many nitrogen products from NO_3RR, including NH_4^+ and NO_2^-, can also modify the interfacial electrolyte environment by buffering the pH and constituting the EDL. However, on the timescale of our GMPNP simulations, we found that such modifications introduced by nitrogen products are likely to be insignificant. First, the diffusive driving force shortens the residence time of NH_4^+ and NO_2^- in the EDL before being transported into the diffusion layer, and their homogeneous acid-base equilibria during the short stay are outpaced by the production of OH^- in NO_3RR, leading to little buffering effect in the EDL region. Second, concentrations of NH_4^+ and NO_2^- and their conjugate acid-base pairs, are orders of magnitude lower than those of the background ions, contributing negligibly to the EDL structure (**Fig. S23–S24**). The NH_3/NH_4^+ equilibria results in both NH_4^+ and NH_3 concentrations being $O(10^{-4})$ M, whereas NO_2^- is very nearly depleted ($C_{NO_2^-}$ ~$O(10^{-6})$ M) because the equilibrium heavily favors HNO_2 formation (C_{HNO_2} ~$O(10^{-4})$ M). Across different flow rates, nitrogen product concentration profiles exhibit the same trend as their corresponding partial current densities. Essentially, we viewed the simulated nitrogen product profiles as the consequence, rather than the cause, of the experimentally observed NO_3RR performance.

To summarize, GMPNP simulations reproduced the interfacial electrolyte environment that exhibits a layered structure. With increasing electrolyte flow rate, the diffusion layer shrinks, enhancing the nitrate diffusion driving force and consequently the NO_3RR activity. But the

compact EDL structure (size and composition) remains almost unperturbed, in line with the experimental observation that the NO_3RR product portfolio was largely unaltered by the flow rate. Meanwhile, the interfacial environment becomes more alkaline due to the higher total current density, hypothetically shifting the NO_3RR selectivity towards nitrite.

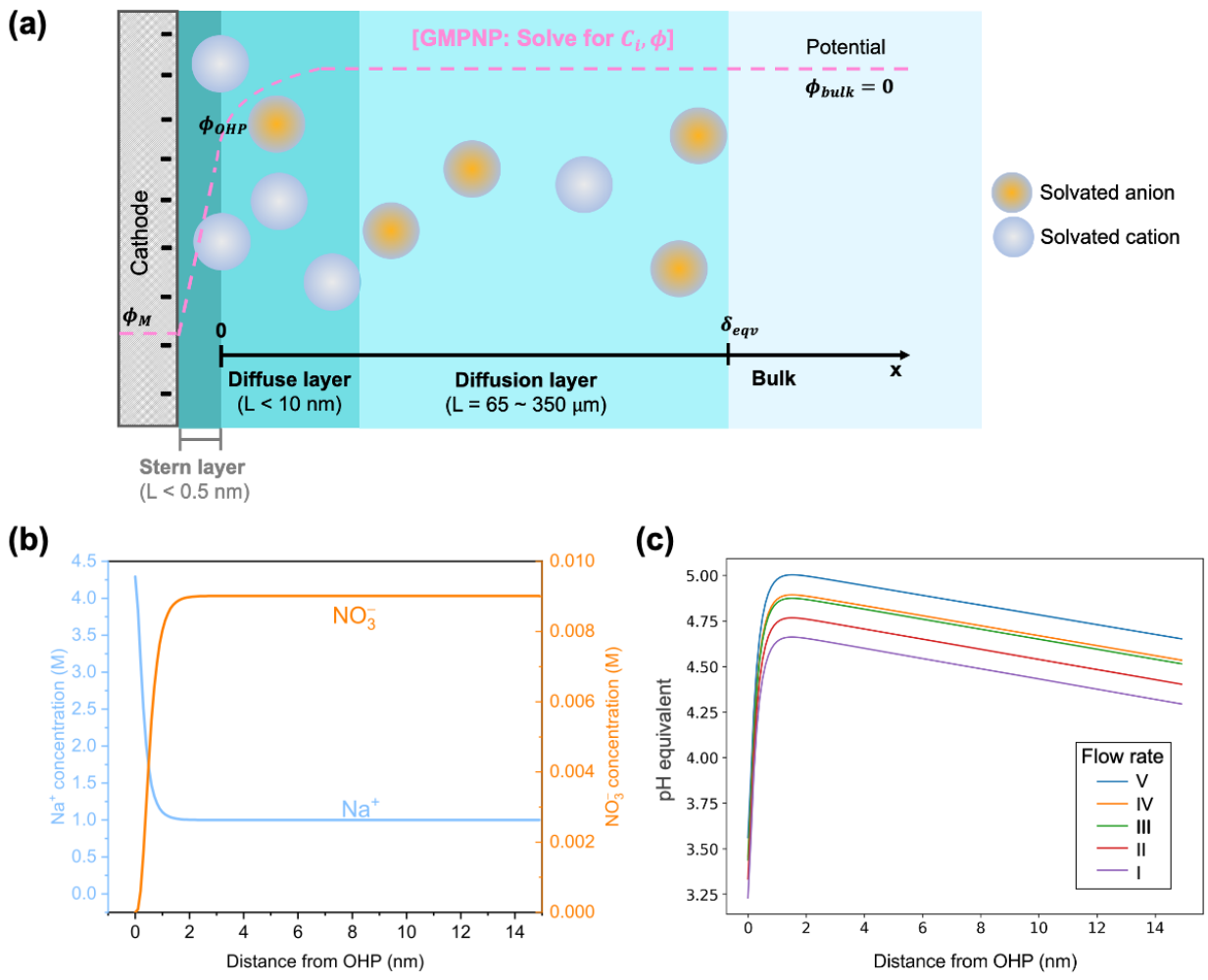

Fig. 2 Computational simulation of interfacial electrolyte properties under different flow rates. (a) Schematic of the different mass transport regions simulated in the GMPNP model. The

EDL consists of Stern layer (also known as the Helmholtz layer, contains specifically adsorbed species) and the diffuse layer. The origin of the x-axis is located at the OHP. GMPNP simulated **(b)** profiles of Na^+ concentration (left axis) and nitrate concentration (right axis) under flow rate V, and **(c)** profiles of pH-equivalent under flow rate I–V in the diffuse layer. All simulations were conducted in 1 M $NaClO_4$ + 10 mM HNO_3 at –1.0 V_{RHE}, using electrochemical results from potentiostatic experiments with a fixed recirculation event number as inputs (same as **Fig. 1**). Complementary simulation results plotted at different distance scales and for other interfacial electrolyte properties are shown in SI **Section S3.1.5**.

How do interfacial electrolyte properties influence NO_3RR performance?

Although GMPNP simulations add microscopic insights to the reaction microenvironment during NO_3RR, they provide only hypotheses regarding the selectivity trend. On one hand, the flow rate dependence of pH-equivalent agreed with that of N-selectivity$_{NH_3}$/N-selectivity$_{NO_2^-}$, indicating that interfacial pH mediates the nitrogen product selectivity. On the other hand, despite being unaltered by the flow rate, the extremely high interfacial Na^+ concentration can also profoundly impact reaction mechanisms.[13,23,24,27,53] Therefore, to examine hypotheses on the origin of mass transport effects on NO_3RR selectivity, we sought to elucidate specific influences of interfacial pH and Na^+ concentration. We intentionally tuned bulk electrolyte compositions to vary the interfacial electrolyte properties, and compared NO_3RR performance under the same mass transport conditions. GMPNP simulations, ATR–SEIRAS measurements, and pulsed potential experiments were leveraged to explicitly identify contributions from different interfacial properties.

Background electrolyte concentration governs the NO_3RR activity

To investigate the influence of interfacial cation concentration on NO_3RR performance without introducing another cationic species, we varied the background electrolyte concentration. With dilute feedstocks as our treatment targets, we investigated the scenario where the background electrolyte concentration was equimolar with the reactant nitrate (10 mM $NaClO_4$ + 10 mM HNO_3, referred to as the dilute background) at the same potential (–1.0 V_{RHE}) and under flow rates II, III and V; complementary GMPNP simulations were performed to characterize the new interfacial electrolyte environment. Simulations revealed a similar accumulation of Na^+ at the OHP, but the steric limit is not reached and the interfacial Na^+ concentration is about 9 times lower than in the concentrated background (**Fig. S25c**). Furthermore, the dilute background dramatically changes the EDL structure. The EDL becomes more disperse, with the diffuse layer extending to *ca.* 10 nm from the OHP due to the lower total concentration of all ionic species. Due to equimolar HNO_3 and background electrolyte, NO_3^- and H^+ become more significant EDL constituents (**Fig. S29**). However, the interfacial pH-equivalent remains on the same order of magnitude and shows a similar flow rate dependence with that in the concentrated background (**Fig. S27**, higher local pH at higher flow rate).

Despite this 9-times lower interfacial Na^+ concentration, experimentally measured NO_3RR selectivity was not significantly affected by the background electrolyte concentration. In the dilute background, nitrite remained the predominant nitrogen product across all flow rates (**Fig. S32d**) with similar N-selectivity$_{NH_3}$/N-selectivity$_{NO_2^-}$ to concentrated background experiments under the same flow rate (**Fig. 3a**). Given the substantial impacts cations could introduce to reaction

energetics (by modifying the electric field or interacting with reaction intermediates),[23,24,47] this insensitivity of nitrogen product distribution to the interfacial Na^+ concentration implied that on Ti, the further reduction of nitrite to various nitrogen products (including ammonia) is not controlled by intermediate adsorption energy.[3,6] The experimentally observed insensitivity of nitrogen product distribution also suggested that potential pH-modifying effects from cations (e.g., hydrolysis of their solvation shells[23]) are not significant enough to shift NO_3RR selectivity under mass transport limitations.

Although the hypothesized cation effects on NO_3RR selectivity were not observed, the NO_3RR activity differed drastically between the dilute and concentrated background experiments. Under the same flow rate, both the time-averaged nitrate removal rate (**Fig. 3b)** and total current density (**Fig. S32a**) in the dilute background were less than half of the values in the concentrated background. This greatly lowered NO_3RR activity could not be completely explained by the loss of applied potential to the higher uncompensated solution resistance in the dilute background (i.e., Ohmic drop, SI **Section S3.2.2**). The activity difference was also not introduced by enhanced competition from HER (**Fig. S32b**), as was found in some CO_2RR cases.[31,54] Instead, combined adverse effects from a higher nitrate mass transport resistance (**Fig. S30**) and a lower interfacial Na^+ concentration were likely accountable. Because the rate determining step (RDS) in NO_3RR on most metals is the adsorption of nitrate and its ensuing reduction into nitrite,[2,3,5,6] and cations can facilitate the RDS by forming ion pairs with nitrate[27] or stabilizing intermediate states,[23,24,51] the significantly lower interfacial Na^+ concentration could lower the NO_3RR activity.

For dependence on the electrolyte flow rate, the dilute background shared similar trends with the concentrated background for both NO_3RR activity and selectivity. Overall, these results suggested that while the background electrolyte concentration directly influences the EDL structure and governs the NO_3RR activity, interfacial cation concentration is not the principal factor in determining the NO_3RR selectivity. Thus, we speculated that the interfacial pH steers the NO_3RR selectivity.

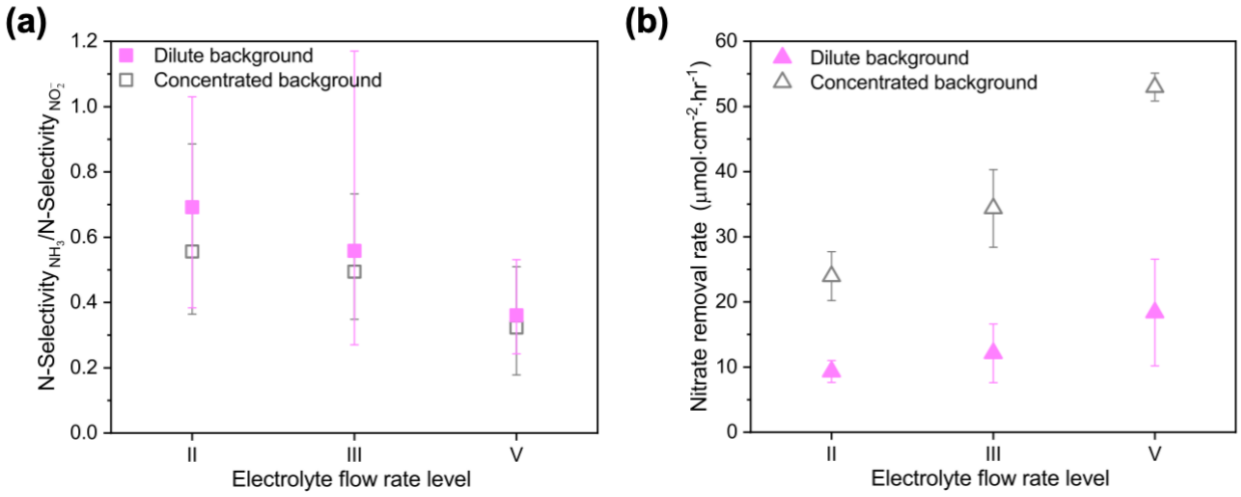

Fig. 3 Background electrolyte concentration effects. Comparison of 30-min potentiostatic experiment (–1.0 V_{RHE}) results in dilute (magenta, filled) and concentrated backgrounds (grey, unfilled), **(a)** ammonia to nitrite N-selectivity ratio, and **(b)** time-averaged nitrate removal rate as functions of electrolyte flow rate. Dilute background: 10 mM $NaClO_4$ + 10 mM HNO_3, concentrated background: 1 M $NaClO_4$ + 10 mM HNO_3. Asymmetric error bars in (a) come from propagating errors in ammonia and nitrite N-selectivity; error bars in (b) represent ± one standard deviation.

Interfacial pH steers the NO_3RR selectivity

To experimentally investigate how the interfacial pH influences NO_3RR, we attempted to maintain the interfacial pH close to the bulk pH by adding phosphate buffer and varied the bulk pH by varying phosphate buffer compositions. We used three 0.5 M phosphate buffers with pH 1.7, 6.5, and 10.5 as electrolytes (referred to as acidic, neutral, and basic phosphate buffers, respectively), while keeping nitrate concentration constant (10 mM) and Na^+ concentration as close to the concentrated background electrolyte as possible (compositions in **Table S3**). Potentiostatic experiments were conducted at the same applied potential (–1.0 V_{RHE}) and under the intermediate flow rate III. Although the increase in the bulk pH after 30-min experiments was at most 1.3 units in all three buffers (**Fig. S33a**), *in situ* pH measurements demonstrated limited buffering effects of phosphate species on the interfacial pH.

We leveraged the surface-sensitive feature of ATR–SEIRAS to measure *in situ* pH via phosphate speciation at the electrode-electrolyte interface under reaction conditions. By determining the ratio of phosphate species, ATR–SEIRAS probed the average pH in the first 5 to 10 nm of stagnant electrolyte[43,55,56] from a Cu electrode under NO_3RR conditions (see **Methods**). Despite difference in cell configuration and NO_3RR performance on Cu and Ti,[36] ATR–SEIRAS experiments provide relatable insights that explain our experimental results on Ti. Under applied potentials more negative than –0.6 V_{RHE}, the interfacial pH was much higher than the bulk pH (**Fig. 4a**); furthermore, the surge in the interfacial pH was nearly instantaneous upon the application of potential (**Fig. S35**). The local alkalinization was drastic enough that the interfacial pH exceeded 12 under –1.0 V_{RHE} in the neutral buffer, aligning with previous observations.[55] Nonetheless, the measured interfacial pH was consistently lower in the acidic buffer than in the neutral buffer under

the same applied potential. These *in situ* pH measurements revealed that, among flow-cell experiments, the interfacial pH was uniformly higher than the bulk pH and expected to follow the trend of acidic buffer < neutral buffer < basic buffer during NO_3RR. Notably, the final bulk pH in the non-buffered concentrated background experiment (30 min, flow rate III) exceeded that in the basic buffer experiment. Thus, the interfacial pH in the non-buffered experiment was likely the highest, surpassing the basic buffer for the majority of the NO_3RR duration.

Building on this trend, we analyzed effects of the interfacial pH on NO_3RR performance across flow-cell experiments in phosphate buffers and the non-buffered concentrated background. Strikingly, we found that HER outcompeted NO_3RR to be the major electrode reaction in all three phosphate buffers (FE_{H_2} > 50%, **Fig. S33c**), with the H_2 partial current density being two orders of magnitude higher than in the non-buffered electrolyte. This substantial enhancement of HER could result from two factors: (1) phosphate species act as buffers that lower the interfacial pH which increases the surface coverage of $H_{(ads)}$ and the thermodynamic favorability of H_2 formation[42] and (2) phosphate species act as exogenous proton donors and contribute to HER through electrochemical deprotonation.[57–59] Despite the likelihood of these qualitative explanations, we refrained from directly connecting HER activity with the interfacial pH. Because the identity and concentration of viable proton donors (e.g., H_3O^+, H_2O, H_3PO_4, $H_2PO_4^-$, HPO_4^{2-}) varied with the interfacial pH, it was not possible to identify the dominant HER mechanisms nor to further deconvolute contributions from the interfacial pH and proton donor speciation on HER activity. Nitrate removal rate was on the same order of magnitude across all three phosphate buffers and the non-buffered electrolytes (**Fig. S33b**), insensitive to both the interfacial pH and proton donor speciation. It could originate from two primary factors: (1) NO_3RR activity was controlled

by mass transport conditions, which was kept constant across the four electrolytes compared, as confirmed by the monotonically increasing trend with the flow rate in the acidic buffer (**Fig. S36**) and (2) it is likely that the elementary step(s) that does not involve protons (e.g., nitrate adsorption, deoxygenation) controls the RDS of NO_3RR on Ti,[3,6,10,42] making it intrinsically less sensitive to the abundance or identity of proton donors compared to reactions where the RDS is controlled by proton-transfer (PT) or concerted proton-electron-transfer (CPET) steps.[57]

In contrast, NO_3RR selectivity varied profoundly across the compared electrolytes. Among the phosphate buffer experiments, the ammonia partial current density increased by about 2.5 times from basic to acidic buffers (**Fig. S34**, whereas the nitrite partial current density was not appreciably different). The observation of acidic conditions favoring ammonia production is consistent with studies on Ti and Cu,[25,26] although our observations of interfacial pH add nuance to previous observations based solely on bulk pH. Additionally, a reaction pathway besides ammonia was facilitated in the basic buffer, signaled by an undetermined nitrogen product(s) comprising 60% of total N-selectivity (**Fig. S33d**). As for the nitrite to ammonia pathway, ammonia was substantially favored in all buffered electrolytes (**Fig. 4b**), with $\text{N-selectivity}_{NH_3}/\text{N-selectivity}_{NO_2^-}$ following the trend: acidic buffer > neutral buffer > basic buffer > 1 (i.e., equimolar ammonia and nitrite produced) > non-buffered. Moving from acidic to basic buffers, as the interfacial pH increased, the N-selectivity ratio gradually approached that in the non-buffered system, which exhibited the highest interfacial pH. Similar trends between the interfacial pH and $\text{N-selectivity}_{NH_3}/\text{N-selectivity}_{NO_2^-}$ once again demonstrated that the interfacial pH is crucial to nitrogen product selectivity. However, like the complication in interpreting HER

activity, because the identity and concentration of viable proton donors differed in phosphate buffers, the proton donor speciation effects on NO_3RR selectivity cannot be excluded.

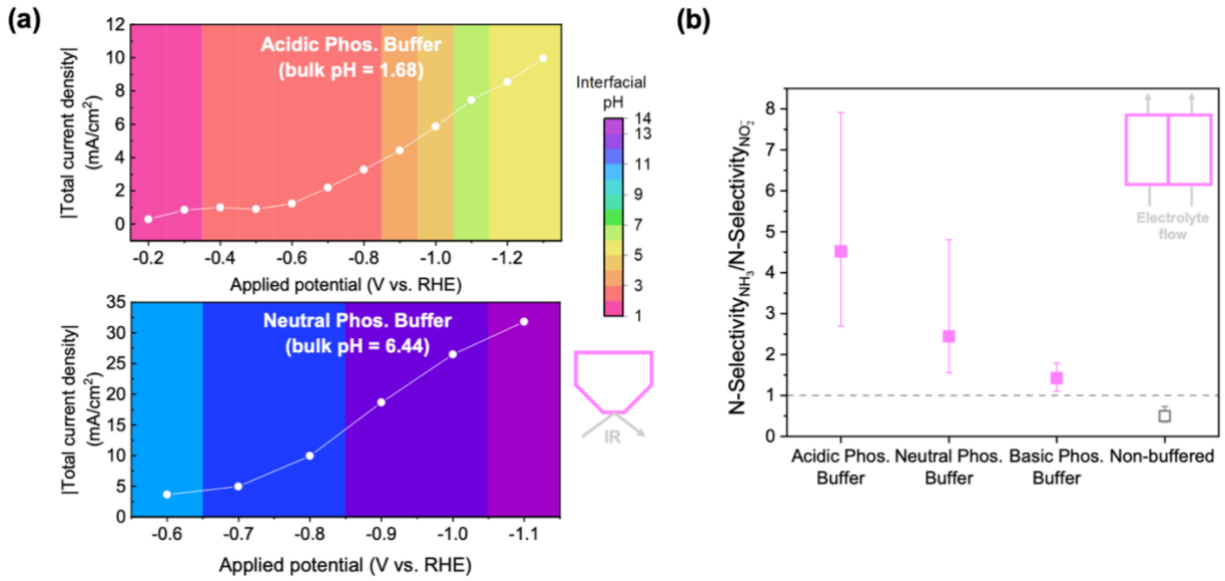

Fig. 4 Interfacial pH effects. (a) Absolute value of total current density (y-axis) and measured interfacial pH (color mapped background) as functions of applied potential in ATR–SEIRAS experiments on Cu electrodes, in acidic and neutral phosphate buffers. (**b**) Comparison of ammonia to nitrite N-selectivity ratios from 30-min potentiostatic (–1.0 V_{RHE}) flow-cell experiments in phosphate buffer (filled) and non-buffered (unfilled) electrolytes. Insets: conceptual diagrams of corresponding cell configurations. Compositions of all electrolytes are given in **Table S3**. Error bars represent ± one standard deviation.

Distinguishing the contribution of interfacial pH on selectivity requires techniques that regulate pH without introducing exogeneous proton donors. Therefore, we applied pulsed potential to periodically replenish the EDL, alleviate the accumulation of OH^-,[22,38,60] and create a less alkaline

interfacial pH environment during NO_3RR. Pulsed potential experiments were conducted in the non-buffered, concentrated background electrolyte under flow rate III. The same cathodic potential (E_C) of –1.0 V_{RHE} was used, and the anodic potential (E_A) was chosen as +0.6 V_{RHE}, slightly below the open circuit potential. Symmetric pulse lengths were applied ($\Delta t_c = \Delta t_A = 10$ s, **Fig. 5a**) that are long enough to fully establish the EDL under NO_3RR conditions (SI **Section S2.3**), and the effective reduction reaction time was kept at 30 min. Drastically different FE and nitrogen product distribution were generated in pulsed potential experiments (**Fig. 5b**). In pulsed potential experiments, HER was substantially enhanced, with FE_{H_2} exceeding 50%; ammonia replaced nitrite as the dominant nitrogen product, and a 3.4-fold N-selectivity$_{NH_3}$/N-selectivity$_{NO_2^-}$ ratio was achieved. Without complications from proton donor speciation, this dramatic change in selectivity of NO_3RR vs. HER and of ammonia vs. nitrite provided strong evidence that a lower interfacial pH primarily accounted for promoting HER and ammonia production in phosphate buffers.

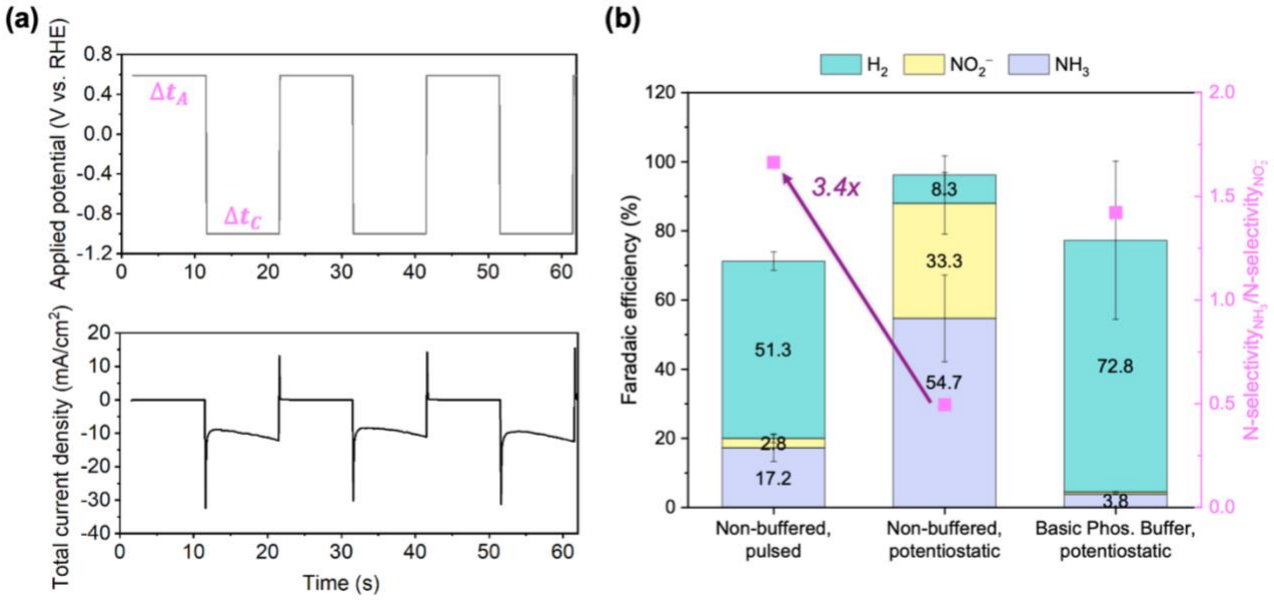

Fig. 5 Pulsed potential experiments. (a) Pattern of applied pulsed potential (top) and current response (bottom). Pulsed potential experiments were conducted in 1 M $NaClO_4$ + 10 mM HNO_3, with E_C = –1.0 V_{RHE}, Δt_C = 10 s, E_A = +0.6 V_{RHE}, Δt_A = 10 s, and total experiment time of 60 min. **(b)** Comparison of Faradaic efficiency (left axis) and ammonia to nitrite N-selectivity ratio (grey squares, right axis) from pulsed potential and potentiostatic experiments under flow rate III. Compositions of all electrolytes are given in **Table S3**. Error bars in (b) represent ± one standard deviation. Error bars on N-selectivity ratios are given in **Fig. S38**.

Combining the flow rate dependence of experimentally measured N-selectivity ratios with pH-equivalent simulated by GMPNP and with *in situ* pH determined by ATR–SEIRAS, we concluded that the interfacial pH is the most likely mediator of mass transport effects on NO_3RR selectivity: higher flow rate led to a higher interfacial pH, favoring nitrite production over ammonia. Because the applied potential was calculated using the initial bulk pH and kept the same throughout

potentiostatic experiments, a higher interfacial pH led to a lower effective potential during experiments, shifting the selectivity towards nitrite.[11,42,61] It is still under debate whether the further reduction of nitrite to ammonia occurs through combination with pre-adsorbed $H_{(ads)}$ or through direct interaction with proton donors (hydronium ions or water in the absence of buffers).[3,10,26,28,35,62] Regardless, a lower interfacial pH corresponds to a higher $H_{(ads)}$ coverage on the electrode surface and/or a higher proton donor concentration near the electrode, promoting the sequential protonation steps beyond nitrite to produce ammonia. Furthermore, we propose that the N-selectivity$_{NH_3}$/N-selectivity$_{NO_2^-}$ ratio acquired from post-experiment bulk phase analysis can be used as a readily accessible indicator of the interfacial pH. While the bulk pH after experiments under different flow rates differed significantly, the corresponding N-selectivity$_{NH_3}$/N-selectivity$_{NO_2^-}$ ratios fell into the same regime (< 1), suggesting that the interfacial pH during NO_3RR was similarly very alkaline for most of the reaction duration. This conclusion aligns with the earlier mentioned observation that water reduction was the main HER mechanism under all flow rates. Similarly, the interfacial pH in the dilute background is likely comparable with that in the concentrated background, whereas pulsed potential likely exhibits an intermediate interfacial pH between basic phosphate buffer and non-buffered potentiostatic experiments. We note that desorption of the reaction intermediate nitrite could also contribute to the N-selectivity change with flow rate, as has been noted on other electrodes with comparable dimensionless nitrite reduction rate constants and mass transfer coefficients.[35] Although nitrite adsorbs favorably on Ti, it is possible that a higher flow rate promotes the nitrite desorption and thus hinders its subsequent reduction to ammonia, by providing a higher diffusion (away) driving force for nitrite or deprotonating the nitric acid produced to form the anionic nitrite that desorbs more easily from the electrode surface. Overall, these results underscore that the interfacial

electrolyte environment differs drastically from the bulk environment and can be engineered to optimize ammonia production.

CONCLUSIONS

In summary, we investigated how mass transport influences NO_3RR performance and elucidated the underlying mechanisms on Ti. By varying the electrolyte flow rate, we systematically controlled the mass transport extent in a flow cell and demonstrated its influence on activity of NO_3RR and HER, as well as selectivity of NO_3RR. With continuum model simulations and ATR–SEIRAS, we characterized the interfacial electrolyte properties and deconvoluted their impacts on experimentally observed mass transport effects. We concluded that the diffusion layer thickness and the interfacial cation concentration govern the NO_3RR activity, whereas the interfacial pH steers the NO_3RR selectivity. Informed by these fundamental insights, we propose engineering strategies to harness mass transport. NO_3RR activity can be enhanced by increasing the mass transport extent and the background electrolyte concentration; ammonia selectivity can be improved by preserving a low interfacial pH, but at the cost of decreased nitrate removal rate or intensified competition from HER. In addition, we have demonstrated that pulsed potential is a powerful technique to tune the interfacial pH without changing the bulk electrolyte composition, which could help interrogate NO_3RR mechanisms and optimize ammonia production.

Although the interfacial cation concentration (0.5–4.3 M Na^+ in this study) was not found to directly influence NO_3RR selectivity, we recognize that cation identity could be impactful, as has been demonstrated in CO_2RR.[13,24,31,52] We also emphasize the need for improved understanding of

the identity and role of proton donors in NO_3RR. In future studies, molecular-scale *operando* spectroscopic techniques (e.g., Fourier-transform infrared spectroscopy, Raman spectroscopy, laser scanning confocal microscopy) and multi-scale computational methods (e.g., GMPNP interfaced with *ab initio* simulations) could enable a molecular view of the dynamic reaction microenvironment in NO_3RR and its influence on reaction energetics. More broadly, this work provides a framework of combined electrochemical experiments, continuum model simulation, and *in situ* infrared spectroscopy to study the interfacial electrolyte environment in the ubiquitous but understudied mass transport-limited regime. Building on mechanistic understanding of mass transport effects in the convenient and representative model reaction of NO_3RR, this study will not only enable rational design of the reaction microenvironment to facilitate sustainable distributed ammonia manufacturing from wastewater, but also provide unique insights on other important energy-relevant electrocatalytic reduction reactions. We believe that understanding and engineering the micro-scale reaction environment present enormous opportunities to help rebalance global biogeochemical cycles for nitrogen, carbon, and beyond.

ACKNOWLEDGEMENTS

We are grateful to several funders of this work, including the National Science Foundation EFRI program (Award 2132007) and the Chemical Engineering Department at Stanford University. J.G. and E.R.C. acknowledge support from the TomKat Center for Sustainable Energy. P.B. acknowledges support from the U.S. Department of Education Graduate Assistance in Areas of National Need Fellowship. M.J.L. acknowledges support from the National Aeronautics and Space Administration (NASA) Space Technology Graduate Research Opportunities fellowship (Award 80NSSC20K1207). Part of this work was performed at the Stanford Nano Shared Facilities (SNSF),

supported by the National Science Foundation under award ECCS-2026822. This work utilized the Summit supercomputer, which is supported by the National Science Foundation (awards ACI-1532235 and ACI-1532236), the University of Colorado Boulder, and Colorado State University. The authors thank Dean M. Miller for support on the RDE setup, wastewater composition table, and inspiring discussions; Xi Chen for support on prototyping the reactor design; Joakim H. Stenlid and Michael T. Tang for insights on reaction mechanisms from the DFT perspective; Ankur Gupta and Charles B. Musgrave for enlightening discussions and feedback throughout the period of this work; and the Tarpeh group for critical feedback on the project.

SUPPORTING INFORMATION

Experimental details; supporting tables; data processing and fitting; simulation model details; and additional experimental and simulation data (PDF)

GMPNP model scripts (temporarily provided as PDF, will publish on Github)

REFERENCES

(1) Abascal, E.; Gómez-Coma, L.; Ortiz, I.; Ortiz, A. Global Diagnosis of Nitrate Pollution in Groundwater and Review of Removal Technologies. *Science of The Total Environment* **2022**, *810*, 152233. https://doi.org/10.1016/j.scitotenv.2021.152233.

(2) Garcia-Segura, S.; Lanzarini-Lopes, M.; Hristovski, K.; Westerhoff, P. Electrocatalytic Reduction of Nitrate: Fundamentals to Full-Scale Water Treatment Applications. *Applied Catalysis B: Environmental* **2018**, *236*, 546–568. https://doi.org/10.1016/j.apcatb.2018.05.041.

(3) Wang, Z.; Richards, D.; Singh, N. Recent Discoveries in the Reaction Mechanism of Heterogeneous Electrocatalytic Nitrate Reduction. *Catal. Sci. Technol.* **2021**, *11* (3), 705–725. https://doi.org/10.1039/D0CY02025G.

(4) van Langevelde, P. H.; Katsounaros, I.; Koper, M. T. M. Electrocatalytic Nitrate Reduction for Sustainable Ammonia Production. *Joule* **2021**, *5* (2), 290–294. https://doi.org/10.1016/j.joule.2020.12.025.

(5) Zeng, Y.; Priest, C.; Wang, G.; Wu, G. Restoring the Nitrogen Cycle by Electrochemical Reduction of Nitrate: Progress and Prospects. *Small Methods* **2020**, *4* (12), 2000672. https://doi.org/10.1002/smtd.202000672.

(6) Wang, Y.; Wang, C.; Li, M.; Yu, Y.; Zhang, B. Nitrate Electroreduction: Mechanism Insight, in Situ Characterization, Performance Evaluation, and Challenges. *Chemical Society Reviews* **2021**, *50* (12), 6720–6733. https://doi.org/10.1039/D1CS00116G.

(7) Galloway, J. N.; Townsend, A. R.; Erisman, J. W.; Bekunda, M.; Cai, Z.; Freney, J. R.; Martinelli, L. A.; Seitzinger, S. P.; Sutton, M. A. Transformation of the Nitrogen Cycle: Recent Trends, Questions, and Potential Solutions. *Science* **2008**, *320* (5878), 889–892. https://doi.org/10.1126/science.1136674.

(8) Tarpeh, W. A.; Chen, X. Making Wastewater Obsolete: Selective Separations to Enable Circular Water Treatment. *Environmental Science and Ecotechnology* **2021**, *5*, 100078. https://doi.org/10.1016/j.ese.2021.100078.

(9) Singh, N.; Goldsmith, B. R. Role of Electrocatalysis in the Remediation of Water Pollutants. *ACS Catal.* **2020**, *10* (5), 3365–3371. https://doi.org/10.1021/acscatal.9b04167.

(10) Anastasiadou, D.; van Beek, Y.; Hensen, E. J. M.; Costa Figueiredo, M. Ammonia Electrocatalytic Synthesis from Nitrate. *Electrochemical Science Advances n/a* (n/a), e2100220. https://doi.org/10.1002/elsa.202100220.

(11) Yu, S.; Louisia, S.; Yang, P. The Interactive Dynamics of Nanocatalyst Structure and Microenvironment during Electrochemical CO2 Conversion. *JACS Au* **2022**, *2* (3), 562–572. https://doi.org/10.1021/jacsau.1c00562.

(12) Banerjee, S.; Gerke, C. S.; Thoi, V. S. Guiding CO2RR Selectivity by Compositional Tuning in the Electrochemical Double Layer. *Acc. Chem. Res.* **2022**, *55* (4), 504–515. https://doi.org/10.1021/acs.accounts.1c00680.

(13) Ringe, S.; Clark, E. L.; Resasco, J.; Walton, A.; Seger, B.; Bell, A. T.; Chan, K. Understanding Cation Effects in Electrochemical CO2 Reduction. *Energy Environ. Sci.* **2019**, *12* (10), 3001–3014. https://doi.org/10.1039/C9EE01341E.

(14) Fan, Q.; Bao, G.; Chen, X.; Meng, Y.; Zhang, S.; Ma, X. Iron Nanoparticles Tuned to Catalyze CO2 Electroreduction in Acidic Solutions through Chemical Microenvironment Engineering. *ACS Catal.* **2022**, 7517–7523. https://doi.org/10.1021/acscatal.2c01890.

(15) Louisia, S.; Kim, D.; Li, Y.; Gao, M.; Yu, S.; Roh, I.; Yang, P. The Presence and Role of the Intermediary CO Reservoir in Heterogeneous Electroreduction of CO2. *Proceedings of the National Academy of Sciences* **2022**, *119* (18), e2201922119. https://doi.org/10.1073/pnas.2201922119.
(16) Seh, Z. W.; Kibsgaard, J.; Dickens, C. F.; Chorkendorff, I.; Nørskov, J. K.; Jaramillo, T. F. Combining Theory and Experiment in Electrocatalysis: Insights into Materials Design. *Science* **2017**, *355* (6321), eaad4998. https://doi.org/10.1126/science.aad4998.
(17) Deng, B.; Huang, M.; Zhao, X.; Mou, S.; Dong, F. Interfacial Electrolyte Effects on Electrocatalytic CO2 Reduction. *ACS Catal.* **2022**, *12* (1), 331–362. https://doi.org/10.1021/acscatal.1c03501.
(18) Bui, J. C.; Kim, C.; King, A. J.; Romiluyi, O.; Kusoglu, A.; Weber, A. Z.; Bell, A. T. Engineering Catalyst–Electrolyte Microenvironments to Optimize the Activity and Selectivity for the Electrochemical Reduction of CO2 on Cu and Ag. *Acc. Chem. Res.* **2022**, *55* (4), 484–494. https://doi.org/10.1021/acs.accounts.1c00650.
(19) Ruggiero, B. N.; Sanroman Gutierrez, K. M.; George, J. D.; Mangan, N. M.; Notestein, J. M.; Seitz, L. C. Probing the Relationship between Bulk and Local Environments to Understand Impacts on Electrocatalytic Oxygen Reduction Reaction. *Journal of Catalysis* **2022**, *414*, 33–43. https://doi.org/10.1016/j.jcat.2022.08.025.
(20) Shih, A. J.; Arulmozhi, N.; Koper, M. T. M. Electrocatalysis under Cover: Enhanced Hydrogen Evolution via Defective Graphene-Covered Pt(111). *ACS Catal.* **2021**, *11* (17), 10892–10901. https://doi.org/10.1021/acscatal.1c02145.
(21) Bard, A. J.; Faulkner, L. R.; White, H. S. *Electrochemical Methods: Fundamentals and Applications*; John Wiley & Sons, 2022.
(22) Xin, H.; Wang, H.; Zhang, W.; Chen, Y.; Ji, Q.; Zhang, G.; Liu, H.; Taylor, A. D.; Qu, J. In Operando Visualization and Dynamic Manipulation of Electrochemical Processes at the Electrode-Solution Interface. *Angewandte Chemie International Edition n/a* (n/a). https://doi.org/10.1002/anie.202206236.
(23) Waegele, M. M.; Gunathunge, C. M.; Li, J.; Li, X. How Cations Affect the Electric Double Layer and the Rates and Selectivity of Electrocatalytic Processes. *J. Chem. Phys.* **2019**, *151* (16), 160902. https://doi.org/10.1063/1.5124878.
(24) Monteiro, M. C. O.; Dattila, F.; Hagedoorn, B.; García-Muelas, R.; López, N.; Koper, M. T. M. Absence of CO2 Electroreduction on Copper, Gold and Silver Electrodes without Metal Cations in Solution. *Nat Catal* **2021**, *4* (8), 654–662. https://doi.org/10.1038/s41929-021-00655-5.
(25) McEnaney, J. M.; Blair, S. J.; Nielander, A. C.; Schwalbe, J. A.; Koshy, D. M.; Cargnello, M.; Jaramillo, T. F. Electrolyte Engineering for Efficient Electrochemical Nitrate Reduction to Ammonia on a Titanium Electrode. *ACS Sustainable Chem. Eng.* **2020**, *8* (7), 2672–2681. https://doi.org/10.1021/acssuschemeng.9b05983.
(26) Pérez-Gallent, E.; Figueiredo, M. C.; Katsounaros, I.; Koper, M. T. M. Electrocatalytic Reduction of Nitrate on Copper Single Crystals in Acidic and Alkaline Solutions. *Electrochimica Acta* **2017**, *227*, 77–84. https://doi.org/10.1016/j.electacta.2016.12.147.
(27) Katsounaros, I.; Kyriacou, G. Influence of the Concentration and the Nature of the Supporting Electrolyte on the Electrochemical Reduction of Nitrate on Tin Cathode. *Electrochimica Acta* **2007**, *52* (23), 6412–6420. https://doi.org/10.1016/j.electacta.2007.04.050.

(28) Yao, Y.; Zhu, S.; Wang, H.; Li, H.; Shao, M. A Spectroscopic Study of Electrochemical Nitrogen and Nitrate Reduction on Rhodium Surfaces. *Angewandte Chemie International Edition* **2020**, *59* (26), 10479–10483. https://doi.org/10.1002/anie.202003071.
(29) Bohra, D.; H. Chaudhry, J.; Burdyny, T.; A. Pidko, E.; A. Smith, W. Modeling the Electrical Double Layer to Understand the Reaction Environment in a CO 2 Electrocatalytic System. *Energy & Environmental Science* **2019**, *12* (11), 3380–3389. https://doi.org/10.1039/C9EE02485A.
(30) Steinmann, S. N.; Michel, C. How to Gain Atomistic Insights on Reactions at the Water/Solid Interface? *ACS Catal.* **2022**, 6294–6301. https://doi.org/10.1021/acscatal.2c00594.
(31) Gu, J.; Liu, S.; Ni, W.; Ren, W.; Haussener, S.; Hu, X. Modulating Electric Field Distribution by Alkali Cations for CO2 Electroreduction in Strongly Acidic Medium. *Nat Catal* **2022**, *5* (4), 268–276. https://doi.org/10.1038/s41929-022-00761-y.
(32) Jarvey, N.; Henrique, F.; Gupta, A. Ion Transport in an Electrochemical Cell: A Theoretical Framework to Couple Dynamics of Double Layers and Redox Reactions for Multicomponent Electrolyte Solutions. **2022**. https://doi.org/10.48550/arXiv.2206.06535.
(33) Katsounaros, I. On the Assessment of Electrocatalysts for Nitrate Reduction. *Current Opinion in Electrochemistry* **2021**, *28*, 100721. https://doi.org/10.1016/j.coelec.2021.100721.
(34) Resasco, J.; Abild-Pedersen, F.; Hahn, C.; Bao, Z.; Koper, M. T. M.; Jaramillo, T. F. Enhancing the Connection between Computation and Experiments in Electrocatalysis. *Nat Catal* **2022**, *5* (5), 374–381. https://doi.org/10.1038/s41929-022-00789-0.
(35) Yan, C.; Kakuturu, S.; Butzlaff, A. H.; Cwiertny, D. M.; Mubeen, S.; Werth, C. J. Scalable Reactor Design for Electrocatalytic Nitrite Reduction with Minimal Mass Transfer Limitations. *ACS EST Eng.* **2021**, *1* (2), 204–215. https://doi.org/10.1021/acsestengg.0c00054.
(36) Abdallah, R.; Geneste, F.; Labasque, T.; Djelal, H.; Fourcade, F.; Amrane, A.; Taha, S.; Floner, D. Selective and Quantitative Nitrate Electroreduction to Ammonium Using a Porous Copper Electrode in an Electrochemical Flow Cell. *Journal of Electroanalytical Chemistry* **2014**, *727*, 148–153. https://doi.org/10.1016/j.jelechem.2014.06.016.
(37) Zhang, B. A.; Ozel, T.; Elias, J. S.; Costentin, C.; Nocera, D. G. Interplay of Homogeneous Reactions, Mass Transport, and Kinetics in Determining Selectivity of the Reduction of CO2 on Gold Electrodes. *ACS Cent. Sci.* **2019**, *5* (6), 1097–1105. https://doi.org/10.1021/acscentsci.9b00302.
(38) Hochfilzer, D.; Xu, A.; Sørensen, J. E.; Needham, J. L.; Krempl, K.; Toudahl, K. K.; Kastlunger, G.; Chorkendorff, I.; Chan, K.; Kibsgaard, J. Transients in Electrochemical CO Reduction Explained by Mass Transport of Buffers. *ACS Catal.* **2022**, 5155–5161. https://doi.org/10.1021/acscatal.2c00412.
(39) Jang, J.; Rüscher, M.; Winzely, M.; Morales-Guio, C. G. Gastight Rotating Cylinder Electrode: Toward Decoupling Mass Transport and Intrinsic Kinetics in Electrocatalysis. *AIChE Journal n/a* (n/a), e17605. https://doi.org/10.1002/aic.17605.
(40) Corral, D.; Feaster, J. T.; Sobhani, S.; DeOtte, J. R.; Lee, D. U.; Wong, A. A.; Hamilton, J.; Beck, V. A.; Sarkar, A.; Hahn, C.; Jaramillo, T. F.; Baker, S. E.; Duoss, E. B. Advanced Manufacturing for Electrosynthesis of Fuels and Chemicals from CO2. *Energy Environ. Sci.* **2021**, *14* (5), 3064–3074. https://doi.org/10.1039/D0EE03679J.

(41) O'Dell, J. W. DETERMINATION OF AMMONIA NITROGEN BY SEMI-AUTOMATED COLORIMETRY. In *Methods for the Determination of Metals in Environmental Samples*; Elsevier, 1996; pp 434–448. https://doi.org/10.1016/B978-0-8155-1398-8.50024-0.
(42) Liu, M. J.; Guo, J.; Hoffman, A. S.; Stenlid, J. H.; Tang, M. T.; Corson, E. R.; Stone, K. H.; Abild-Pedersen, F.; Bare, S. R.; Tarpeh, W. A. Catalytic Performance and Near-Surface X-Ray Characterization of Titanium Hydride Electrodes for the Electrochemical Nitrate Reduction Reaction. *J. Am. Chem. Soc.* **2022**, *144* (13), 5739–5744. https://doi.org/10.1021/jacs.2c01274.
(43) Zhumaev, U. E.; Domke, K. F. Surface-Enhanced Infrared Absorption Spectroscopy. In *Encyclopedia of Interfacial Chemistry*; Wandelt, K., Ed.; Elsevier: Oxford, 2018; pp 542–548. https://doi.org/10.1016/B978-0-12-409547-2.13627-3.
(44) Chen, F.-Y.; Wu, Z.-Y.; Gupta, S.; Rivera, D. J.; Lambeets, S. V.; Pecaut, S.; Kim, J. Y. T.; Zhu, P.; Finfrock, Y. Z.; Meira, D. M.; King, G.; Gao, G.; Xu, W.; Cullen, D. A.; Zhou, H.; Han, Y.; Perea, D. E.; Muhich, C. L.; Wang, H. Efficient Conversion of Low-Concentration Nitrate Sources into Ammonia on a Ru-Dispersed Cu Nanowire Electrocatalyst. *Nat. Nanotechnol.* **2022**, 1–9. https://doi.org/10.1038/s41565-022-01121-4.
(45) Dima, G. E.; de Vooys, A. C. A.; Koper, M. T. M. Electrocatalytic Reduction of Nitrate at Low Concentration on Coinage and Transition-Metal Electrodes in Acid Solutions. *Journal of Electroanalytical Chemistry* **2003**, *554–555*, 15–23. https://doi.org/10.1016/S0022-0728(02)01443-2.
(46) Horányi, G.; Rizmayer, E. M. Role of Adsorption Phenomena in the Electrocatalytic Reduction of Nitric Acid at a Platinized Platinum Electrode. *Journal of Electroanalytical Chemistry and Interfacial Electrochemistry* **1982**, *140* (2), 347–366. https://doi.org/10.1016/0022-0728(82)85178-4.
(47) Marcandalli, G.; Monteiro, M. C. O.; Goyal, A.; Koper, M. T. M. Electrolyte Effects on CO2 Electrochemical Reduction to CO. *Acc. Chem. Res.* **2022**. https://doi.org/10.1021/acs.accounts.2c00080.
(48) Wang, H.; Guo, Y.; Li, C.; Yu, H.; Deng, K.; Wang, Z.; Li, X.; Xu, Y.; Wang, L. Cu/CuOx In-Plane Heterostructured Nanosheet Arrays with Rich Oxygen Vacancies Enhance Nitrate Electroreduction to Ammonia. *ACS Appl. Mater. Interfaces* **2022**, *14* (30), 34761–34769. https://doi.org/10.1021/acsami.2c08534.
(49) Wang, C.; Ye, F.; Shen, J.; Xue, K.-H.; Zhu, Y.; Li, C. In Situ Loading of Cu2O Active Sites on Island-like Copper for Efficient Electrochemical Reduction of Nitrate to Ammonia. *ACS Appl. Mater. Interfaces* **2022**. https://doi.org/10.1021/acsami.1c21691.
(50) Resasco, J.; Chen, L. D.; Clark, E.; Tsai, C.; Hahn, C.; Jaramillo, T. F.; Chan, K.; Bell, A. T. Promoter Effects of Alkali Metal Cations on the Electrochemical Reduction of Carbon Dioxide. *J. Am. Chem. Soc.* **2017**, *139* (32), 11277–11287. https://doi.org/10.1021/jacs.7b06765.
(51) Monteiro, M. C. O.; Dattila, F.; López, N.; Koper, M. T. M. The Role of Cation Acidity on the Competition between Hydrogen Evolution and CO2 Reduction on Gold Electrodes. *J. Am. Chem. Soc.* **2022**, *144* (4), 1589–1602. https://doi.org/10.1021/jacs.1c10171.
(52) Garlyyev, B.; Xue, S.; Watzele, S.; Scieszka, D.; Bandarenka, A. S. Influence of the Nature of the Alkali Metal Cations on the Electrical Double-Layer Capacitance of Model Pt(111) and Au(111) Electrodes. *J. Phys. Chem. Lett.* **2018**, *9* (8), 1927–1930. https://doi.org/10.1021/acs.jpclett.8b00610.

(53) Fedurco, M.; Kedzierzawski, P.; Augustynski, J. Effect of Multivalent Cations upon Reduction of Nitrate Ions at the Ag Electrode. *J. Electrochem. Soc.* **1999**, *146* (7), 2569. https://doi.org/10.1149/1.1391973.
(54) Goyal, A.; Koper, M. T. M. The Interrelated Effect of Cations and Electrolyte PH on the Hydrogen Evolution Reaction on Gold Electrodes in Alkaline Media. *Angewandte Chemie International Edition* **2021**, *60* (24), 13452–13462. https://doi.org/10.1002/anie.202102803.
(55) Yang, K.; Kas, R.; Smith, W. A. In Situ Infrared Spectroscopy Reveals Persistent Alkalinity near Electrode Surfaces during CO2 Electroreduction. *J. Am. Chem. Soc.* **2019**, *141* (40), 15891–15900. https://doi.org/10.1021/jacs.9b07000.
(56) Corson, E. R.; Kas, R.; Kostecki, R.; Urban, J. J.; Smith, W. A.; McCloskey, B. D.; Kortlever, R. In Situ ATR–SEIRAS of Carbon Dioxide Reduction at a Plasmonic Silver Cathode. *J. Am. Chem. Soc.* **2020**, *142* (27), 11750–11762. https://doi.org/10.1021/jacs.0c01953.
(57) Jackson, M. N.; Jung, O.; Lamotte, H. C.; Surendranath, Y. Donor-Dependent Promotion of Interfacial Proton-Coupled Electron Transfer in Aqueous Electrocatalysis. *ACS Catal.* **2019**, *9* (4), 3737–3743. https://doi.org/10.1021/acscatal.9b00056.
(58) Da Silva, S.; Basséguy, R.; Bergel, A. Electrochemical Deprotonation of Phosphate on Stainless Steel. *Electrochimica Acta* **2004**, *49* (26), 4553–4561. https://doi.org/10.1016/j.electacta.2004.04.039.
(59) Marcandalli, G.; Boterman, K.; Koper, M. T. M. Understanding Hydrogen Evolution Reaction in Bicarbonate Buffer. *Journal of Catalysis* **2022**, *405*, 346–354. https://doi.org/10.1016/j.jcat.2021.12.012.
(60) Bui, J. C.; Kim, C.; Weber, A. Z.; Bell, A. T. Dynamic Boundary Layer Simulation of Pulsed CO2 Electrolysis on a Copper Catalyst. *ACS Energy Lett.* **2021**, *6* (4), 1181–1188. https://doi.org/10.1021/acsenergylett.1c00364.
(61) Chan, K. A Few Basic Concepts in Electrochemical Carbon Dioxide Reduction. *Nat Commun* **2020**, *11* (1), 5954. https://doi.org/10.1038/s41467-020-19369-6.
(62) Carvalho, O. Q.; Marks, R.; Nguyen, H. K. K.; Vitale-Sullivan, M. E.; Martinez, S. C.; Árnadóttir, L.; Stoerzinger, K. A. Role of Electronic Structure on Nitrate Reduction to Ammonium: A Periodic Journey. *J. Am. Chem. Soc.* **2022**. https://doi.org/10.1021/jacs.2c05673.